

**Unveiling the mechanisms of cold sintering of ZnO at 250 °C by varying applied stress and characterizing grain boundaries by Kelvin Probe Force Microscopy**

J. Gonzalez-Julian,<sup>1\*</sup> K. Neuhaus,<sup>2</sup> M. Bernemann,<sup>2</sup> J. Pereira da Silva,<sup>1</sup> A. Laptev,<sup>1</sup> M. Bram,<sup>1</sup> and O. Guillon<sup>1</sup>

<sup>1</sup> Forschungszentrum Jülich GmbH, Institute of Energy and Climate Research: Materials Synthesis and Processing (IEK-1), 52425 Jülich, Germany.

<sup>2</sup> Institute for Inorganic and Analytical Chemistry, University of Münster, Corrensstr. 28/30, D-48149 Münster, Germany.

\* Corresponding author

**Abstract**

The sintering behavior of nanocrystalline ZnO was investigated at only 250 °C. Densification was achieved by the combined effect of uniaxial pressure and the addition of water both in a Field Assisted Sintering Technology/Spark Plasma Sintering apparatus and a ~~warm~~ hand press with a heater holder. The final pure ZnO materials present high densities (> 90 % theoretical density) with nano-grain sizes. By measuring the shrinkage rate as a function of applied stress it was possible to identify the stress exponent related to the densification process. A value larger than one points to non-linear relationship going beyond single solid-state diffusion or liquid phase sintering. Only a low amount of water (1.7 wt.%) was needed since the process is dictated by the adsorption on the surface of the ZnO particles. Part of the adsorbed water dissociates into  $H^+$  and  $OH^-$  ions, which diffuse into the ZnO crystal structure, generating grain boundaries/interfaces with high defect chemistry. As characterized by Kelvin Probe Force Microscopy, and supported by impedance spectroscopy, this highly defective grain boundary area presents much higher surface energy than the bulk. This highly defective grain boundary

area with high potential reduces the activation energy of the atomic diffusion, leading to sinter the compound at low temperature.

## **1. Introduction**

Reduction of the sintering temperature and time required to tailor the microstructure – and therefore the properties – and save energy has been, is and will be one of the major concerns of the ceramic industry. High temperatures ( $> 1000\text{ }^{\circ}\text{C}$ ) are typically required to fully densify ceramics, limiting the design of the microstructure due to different effects, such as phase transformation, melting, migration of elements of the crystal structure, volatility, reactions between phases, and/or grain growth [1]. In addition, the high temperature entails large economic and environmental costs to industry and society. As an example, above 7 % of the total primary energy in Germany is used for industrial heat treatments above  $1000\text{ }^{\circ}\text{C}$  to produce metal, cermet and ceramic products.

Several approaches have thus been proposed to reduce the sintering temperature. These strategies can be classified in three main categories: i) optimization of the powders, ii) addition of sintering aids and iii) development of advanced sintering techniques. Refining of the starting powder to decrease the diffusion distance of mobile chemical species and therefore increase the densification rate [2], as well as to remove surface oxides in non-oxide ceramics [3], are well known methods to reduce the sintering temperature. Addition of second phases into the starting composition is also a well-established approach to reduce the sintering temperature of ceramic compounds. These sintering aids can be added to eliminate the oxide surface layer that cover the non-oxide ceramic particles and hinder densification. However, the sintering additives

are more commonly incorporated to form a liquid phase between the particles at high temperature, which generates capillary forces and increases the diffusion rates by partial dissolution of the solid phase and transport through the liquid [4]. This process is known as liquid phase sintering (LPS), and is widely used in industry. However, the solidified second phase remains in the microstructure – typically at grain boundaries – altering the final properties of the material. Regarding the sintering techniques, a significant progress has been achieved in the last decades. Hot isostatic pressing (HIP), Hot-pressing (HP), Field Assisted Sintering Technology/Spark Plasma Sintering (FAST/SPS) and the recent flash sintering (FS) enable to reduce by hundreds of degrees the furnace temperature [5][6]. These techniques are assisted by pressure and/or by electric current and field. As a result, new functionally graded ceramic materials, composites, transparent or non-equilibrium materials can be fully densified. A combination of these three main approaches – refining of powder, use of additives and sintering technique – is particularly appealing to reduce the sintering temperature and tailor the microstructure.

In principle, water would be a perfect sintering aid due to its abundance, low price, safety, easy handling and environmentally-friendly nature. However, the role of water as sintering additive or in the sintering atmosphere has hardly been considered for the densification of ceramic materials due to its low boiling point (100 °C at 1 atm.) in comparison with the required high temperatures (> 1000 °C). As a result, water is usually evaporated before sintering starts. Nevertheless, it has been shown that densification can be enhanced by water by different approaches.

Developed in Japan, hydrothermal hot-pressing is based on an autoclave that is externally heated [7], the powder with a proper content of water being placed between two pistons, which transmit uniaxial pressure. The pistons have a space for the release of water included in the starting powder. This space is required to remove the water present in the pore volume of the powder compact that hinders further compaction. As a result, steam pressure in autoclave is kept, while the powder is heated and compressed by the pushrods. This method has two characteristics: i) continuous compression of the powder under hydrothermal conditions, and ii) removal of water from the interstices of the powder grains in to the autoclave free space. The processing parameters in hydrothermal hot pressing are maximal temperature of 300 °C, heating rates of 10 °C/min, pressure of 40 MPa and dwell time of 2 hours. Under these conditions, borosilicate glass was fully densified because water diffused into the particles [8], but on the other hand, silica and amorphous titania remained porous [8][9]. Nevertheless, dense hydroxyapatite ceramics were obtained by hydrothermal hot-pressing, but promoting hydrothermal reactions through the incorporation of precursor compounds [10]. Zeolite compounds were sintered by hydrothermal hot-pressing containing 17 wt.% of water with different amounts of NaOH (final molar solutions of 0.1 – 10M) [11], suggesting dissolution and precipitation as the consolidation mechanism.

In 2007, “cold sintering” of  $\text{CaCO}_3$  was demonstrated at room temperature, using the combined action of mechanical pressure,  $\text{CO}_2$  gas pressure and time [12]. It was proposed that the amount of dissolved limestone available for the reprecipitation is an important factor determining the efficiency of the process and the increase in mechanical strength. High  $\text{CO}_2$ -

pressure combined with high mechanical pressure facilitates the formation of a new calcium carbonate phase that binds the powder particles to an agglomerate.

Another related approach using Field Assisted Sintering Technology / Spark Plasma Sintering has reported by Schwarz et al.[13] in 2012. The possibility of using high heating rates (100°C/min) in this kind of equipment enabled the densification of humid ZnO powder already above 200°C under 50 MPa. Densification was completed after 10 min at a temperature of 400°C, whereas a dry powder hardly sintered. Similarly, slow heating rates did not enable to achieve relative densities higher than ~ 65%. Dargatz et al.[14][15] investigated further in great detail this phenomenon, so that highly dense ZnO (99,5 %) with a mean grain size of 200 nm was obtained at 400°C. A controlled, small amount of water (< 7.7 wt.%, optimized at 1.6 wt.%) was directly added into the green compact. This water had no time to fully evaporate during heating in the graphite die and therefore got trapped at the surface and grain boundaries, with the following consequences: removal of carbonates on the particle surface, dissolution of  $\text{Zn}^{2+}$  and  $\text{O}^{2-}$  ions, mass transport through the liquid phase, and diffusion of  $\text{H}^+$  and  $\text{OH}^-$  ions into the crystal structure of ZnO. It was clearly demonstrated that the electric field does not play any role in this process, but the addition of zinc oxide precursors such as zinc acetate considerably fostered densification. In addition, a change in the electrical properties was reported and proton conductivity was observed for the water-containing specimens.

Water assisted sintering was further recently used for densification of several ceramic compounds at very low temperature (< 300 °C) by Randall et al.[16][17][18] naming the process “Cold Sintering Process” (CSP). The basic principle is hardly different from the works published before. It is based on the densification of moistened ceramic powders under very high uniaxial

pressures (up to 570 MPa, in contrast to a few tens of MPa in the other references), hence reducing the maximal required temperatures ( $< 200\text{ }^{\circ}\text{C}$ ). As for every pressure-assisted sintering technology, it is well-known that the external compressive stress is an additional driving force for densification, either accelerating existing densification mechanisms or even triggering new ones [1]. The moistened ceramics pellets were obtained either by mixing the powder with water (typically 4-25 wt.%, i.e. even higher volume content) or storing the powder into a humidity chamber [19], as in [13]. The drastically reduced temperatures enable to use simple ~~warm~~ hand press equipment with a heater holder, which is for sure an advantage. CSP was also demonstrated for ZnO [20], where addition of acetic acid into the aqueous solution dramatically changed the final density and microstructure. In that work, ZnO with theoretical densities higher than 90% was obtained at  $< 300\text{ }^{\circ}\text{C}$ , showing equivalent electrical conductivities as for ZnO sintered at higher temperatures by conventional sintering. CSP is thought to be based on liquid phase sintering mechanisms – particle rearrangement and dissolution-precipitation stages –, which creates a supersaturated environment and enables a fast precipitation process on the particle surfaces to reach the final densification. Nevertheless, for some materials like zirconia, CSP is more a compaction process than sintering, and a further thermal treatment at higher temperature is required to fully crystallize the material [19][21]. On the other hand, other materials such as  $\text{Li}_2\text{MoO}_4$ -based composites can be densified at room temperature using its water solubility, high pressure and a post-processing at  $120\text{ }^{\circ}\text{C}$  [22]. Furthermore, a novel process combining CSP and flash sintering has been recently reported by J. Nie et al. [23]. The combination of both methods leads to achieve ZnO materials with theoretical densities around 98% in wet Ar + 5%  $\text{H}_2$  without any external furnace heating. Again,

water plays a determinant role since its absorption on the ZnO nano-particles increased more than 10.000 times the electrical conductivity of the green body, enabling the room temperature flash.

All these studies suggest that the presence of water can, under given conditions, strongly reduce the sintering temperature of oxide powder compacts, by partial dissolution of the particles and subsequent precipitation, synthesis reaction or the diffusion of ions from the water molecules into the crystal structure [17][14][24]. Nevertheless, more fundamental investigations are required that is also the scope of the present paper.

The aim of the present work is to understand the mechanisms that control the sintering process in order to reduce even more the maximal temperature for the densification of ceramic compounds. We use FAST/SPS as a reproducible and controlled tool for quantifying the role of pressure. Kelvin Probe Force Microscopy is carried out to get valuable information on local defect chemistry and properties of bulk and grain boundaries, which enables to further rationalize the effect of water. ZnO was chosen as reference material in order to directly correlate our results to previous studies, but the method and mechanisms are expected to be transferred to other hydrophilic ceramic materials.

## **2. Experimental**

Commercial ZnO powder (NG20, Nanogate AG, Quierschied-Göttelborn, Germany) with a purity of > 99.99 wt.% and particle size between 20 and 50 nm was used as starting material. More details about the features and characterization of the starting powder can be found elsewhere [25]. Densification process was performed by FAST/SPS (HP-D5, FCT Systeme, Rauenstein,

Germany) using non-conventional tools to overcome the mechanical restrictions of the standard graphite tools (typically < 100 MPa). In order to further increase the mechanical pressure, a tool made from hot work steel (W-360-Isobloc, Böhler, Germany) was used. The steel punches were thermally treated in vacuum to achieve a hardness of  $53 \pm 2$  HRC. The inner diameter of the die was 20 mm, and the applied pressures were 100 MPa, 125 MPa and 150 MPa in our experiments. Same FAST/SPS experimental procedure in comparison with the conventional graphite tools was carried out with the steel tool. A graphite foil (0.4 mm thickness) was placed in the inner face of the die, and between the down punch and the powder in order to ensure a good mechanical, thermal and electrical contact, as well as to prevent reactions between the die and powders. Then, 3g of ZnO powder were poured into the die and pre-pressed at 16 MPa, followed by the addition of 1.6 wt.% of deionized water into the green body with a micropipette. Besides, in some experiments 0.5 wt.% of zinc acetate (Alfa Aesar, Germany) was previously dissolved in the water. After the addition of water, a graphite foil was rapidly placed between the upper punch and the powder. Finally, the powder was pressed at 50 MPa and positioned into the FAST/SPS chamber. In addition, a blank ZnO specimen based on the as received commercial powder without any treatment or addition of water was similarly processed and sintered for comparison. Sintering parameters were: maximal temperature of 250 °C, heating ramp of 100 °C/min, dwell time of 5 min and vacuum atmosphere in the chamber. Temperature was controlled by a thermocouple (type K), which was located in a hole in the middle of the die with a distance of 5 mm to the sample. The axial displacement was recorded every second during the sintering process by the FAST/SPS equipment with a resolution of 10  $\mu$ m. At least three experiments were done per condition and



composition. All the sintering curves were corrected subtracting the thermal expansion of the steel tools, which was performed by a further thermal treatment of a dense ZnO sample with the same cycle.

As sintering was carried out at a low temperature of only 250 °C, the possibility of transferring the method to a ~~warm~~ hand press with a heater holder (Model 10H, P/O/Weber, Germany) was investigated. The starting composition and the procedure were kept the same as for the FAST/SPS cycles using also steel tools, although some differences in the heating ramp and atmosphere were inevitable due to specificities of the equipment. The sintering parameters were: maximal temperature of 250 °C, heating rate of 20 °C/min, dwell time of 5 min, air atmosphere and uniaxial pressures of 150 and 300 MPa. To summarize, two different conditions for densification were used: i) FAST/SPS using steel tools, and ii) ~~warm~~ hand pressing with a heater holder (WP). In addition, three different ZnO starting compositions were used: i) as-received (ZnO/AR), ii) with water addition (ZnO/H<sub>2</sub>O) and iii) with water and zinc acetate addition (ZnO/Ac-H<sub>2</sub>O).

Bulk densities of the sintered samples were measured by the Archimedes method in water, and relative densities were calculated using the theoretical value of 5.606 g/cm<sup>3</sup>. Phase composition as well as particle and grain sizes were determined by X-ray diffraction (XRD, Advanced Bruker Corporation, Germany). Crystallite size was evaluated by Scherrer analysis for samples with crystal sizes smaller than 100 nm. Fracture surfaces were observed in a scanning electron microscope (SEM, Zeiss Ultra55, Germany). Kelvin Probe Force Microscopy (KPFM, 5500 Keysight, USA) was used to measure the surface potential of the ZnO sintered specimens. Tests

of the reproducibility were performed using a Cypher AFM (Asylum Research, USA). Polished samples were observed using platinum coated probes (by Nanosensors) with < 25 nm diameter. Measurements were executed in amplitude modulation mode (KPFM-AM). At least 100 grains were measured for the calculation of the mean surface potential difference between grains and grain boundaries.

Impedance measurements in ambient air were performed at -20 to 90 °C and back to -20 °C using an Autolab PGSTAT 302N (Metrohm AG, Switzerland) with Nova 1.11 software and a Julabo FP88 thermostate (Julabo GmbH, Germany) for temperature control. Colloidal silver paste (G3692, Acheson) was applied directly on the samples to improve the electrode-sample contact. The paste electrodes were contacted by stainless steel electrodes. An AC peak-to-peak amplitude of 40 mV was applied in the experiments. For every temperature step, three impedance spectra were obtained and an average conductivity was taken for further calculations. The experimental frequency dependence of the impedance was fitted using the software package ZView 2 (Scribner Associates, Inc.). For fitting of the data of ZnO and ZnO/H<sub>2</sub>O, an equivalent circuit with two resistors (R1 and R2) in series, which each have a constant phase element (CPE) in parallel, was used. One resistor/constant phase element can be assigned to bulk characteristics (R1/CPE1) and one to grain boundary characteristics (R2/CPE2), respectively. The resistivity of the sample-electrode interface was negligible in comparison to the resistivity of the samples and was therefore not considered. For ZnO/Ac-H<sub>2</sub>O, the total sample resistivity was much lower and the contact resistance could not be omitted. Therefore, an additional resistor with a CPE in parallel was applied for fitting the measurement results. The grain boundary conductivity values of all samples were corrected

with the factor  $L_{gb}/L_g$  ( $L_g$ : average grain size from AFM measurements, see Tab. II,  $L_{gb}$ : average thickness of the grain boundary, in this case assumed to be 1 nm) to receive the corrected grain boundary conductivity  $\sigma_{gb}^*$  according to the brick layer model [26]. Activation energies were calculated from Arrhenius diagrams of the respective conductivities.

ZnO grains were previously described by a space charge model, where the grain boundaries present a Mott-Schottky type contact [27]. Hence, an approximation of the space charge potential  $\Delta\Phi$ , which is equivalent to the Schottky barrier height at the grain boundaries, can be calculated from the impedance spectroscopy measurements by numerically solving the following equation [28]:

$$\rho_{gb}/\rho_{bulk} = (\exp(2e\Delta\Phi/kT))/(4e\Delta\Phi/kT) \quad (1)$$

Here,  $\rho_{gb}$  is the grain boundary resistivity,  $\rho_{bulk}$  is the bulk resistivity,  $e$  is the elementary charge,  $k$  is the Boltzmann constant in J/K, and  $T$  is the temperature in K. The space charge potential from impedance spectroscopy measurements ( $\Delta\Phi_{imp}$ ) can be related to the potential difference between bulk and grain boundary determined by KPFM measurements ( $\Delta\Phi_{SP}$ ).  $\Delta\Phi_{imp}$  should therefore show a similar trend for the different samples like  $\Delta\Phi_{SP}$ , although we assume  $\Delta\Phi_{imp}$  to be slightly larger than  $\Delta\Phi_{SP}$ , as  $\Delta\Phi_{SP}$  is a mixed signal from the GB interior and the space charge region due to the bluntness of the KPFM tip.

### 3. Results

#### 3.1. Analysis of the sintering behavior and effect of pressure

Densification in FAST/SPS takes place only in the axial direction (lateral shrinkage is negligible) so it can be computed by the following equation [1]:

$$\rho = \rho_0 \exp(-\varepsilon_z) \quad (2)$$

where  $\rho_0$  is the initial density and  $\varepsilon_z$  is the vertical strain. At moderate loads, although larger than the sintering stress, the true strain rate in FAST/SPS can be described by the next equation [1][29]:

$$-\dot{\varepsilon}_z = \frac{1}{\rho} \frac{d\rho}{dt} = \frac{HD(\phi p_a)^n}{G^m kT} \quad (3)$$

where  $\dot{\varepsilon}_z$  is the normalized densification rate,  $H$  is a constant,  $D$  is the diffusion coefficient of the rate-controlling species,  $\phi$  is the stress intensification factor,  $p_a$  is the applied uniaxial pressure,  $n$  is the stress exponent,  $G$  is the grain size,  $m$  is the grain size exponent,  $k$  is a constant and  $T$  is the absolute temperature. The stress intensification factor was used according to Montes et al.[30] for uniaxial compression:

$$\phi = \left[1 - \left(\frac{\theta}{\theta_M}\right)\right]^{-1} \quad (4)$$

where  $\theta_M$  is the minimal equilibrium porosity without deformation, which can be estimated to the green density. Therefore, according to equations (2), (3) and (4), the stress exponent  $n$  can be calculated if grain size and temperature are kept constant, using the following relation [29]:

$$\ln\left(\frac{1}{\rho} \frac{d\rho}{dt}\right) \propto n \cdot \ln(\phi p_a) \quad (G \text{ and } T = \text{const}) \quad (5)$$

As negligible grain growth up to theoretical densities of 93% was observed in a previous work of the co-authors using the same ZnO powder and amount of water [15], the ~~data used~~ density range considered for the calculation of the stress exponent  $n$  was kept ~~below this theoretical density value~~ between 80 and 85%, so that a constant grain size can be guaranteed. This is also confirmed by the present grain size measurements.

In order to unveil the cold sintering mechanisms and to determine the stress exponent, densification behaviour for the different starting compositions sintered by FAST/SPS up to 250 °C under the whole range of applied pressure, between 100 MPa and 150 MPa, is shown in Figure 1. The sintering evolution is much different between the compositions with water (ZnO/H<sub>2</sub>O and ZnO/Ac-H<sub>2</sub>O) and without (ZnO/AR). The first difference resides in the green density, which is larger when the ZnO contains water due to the reduction of the friction between the particles. In addition, the green densities increased with the applied pressure, achieving a maximal value of 59.5 % at 150 MPa. This effect, although not clearly investigated in detail and not modeled, is frequently observed and was already reported for lower pressures [14]. The second difference is clearly observed in the densification behaviour and the final density. ZnO/AR did not significantly densify under these sintering conditions and just achieved a final relative density of 52.0 % at 100 MPa. However, the compositions containing water reached relative densities between 84.1 % and 97.2 %. At 100 MPa (Fig. 1a), ZnO/Ac-H<sub>2</sub>O presented a faster sintering rate during the heating ramp, and the final relative density (88.3%) was higher than the ZnO/H<sub>2</sub>O (84.1%). As expected, the applied pressure plays a critical role in the densification behaviour at low temperatures. When the pressure was increased, Fig 1b and c, the difference in the final densities between ZnO/Ac-H<sub>2</sub>O and ZnO/H<sub>2</sub>O was larger.

Interestingly, the compressive stress is also determinant for the onset of the densification. Figure 2 shows the onset temperature for the densification of ZnO/H<sub>2</sub>O and ZnO/Ac-H<sub>2</sub>O as a function of the applied pressure, including the value at 50 MPa under the same sintering conditions as reported by Dargatz et al. [14]. This onset temperature was defined as the lowest temperature at which the axial displacement is larger than 60 µm in a period of 10 s. Interestingly, the onset temperature is completely different for both compositions containing water. ZnO/H<sub>2</sub>O presented a clear decrease of the onset temperature from 130 °C to 89°C with the increase of the applied pressure in the range between 50 MPa and 150 MPa. The reduction of the temperature is rather high, and indicates a decisive role of the applied pressure to densify ZnO at low temperature. On the other hand, with the presence of the acetate, ZnO/Ac-H<sub>2</sub>O started to densify from room temperature, whatever the applied stress had been. Certainly, the strong reduction of the onset temperature – or even elimination since densification started at room temperature - by the acetate is determinant to achieve high final densities at low temperature.

Nevertheless, pressure is not the only factor to densify ZnO at low temperature. Part of the added water was dissociated and diffused in the ZnO grains – as will be explained later in the *discussion* section – and the other part was evaporated and monitored by the gas pressure in the FAST/SPS chamber (Supplementary data 1). It has to be mentioned that the change in the gas pressure of the chamber can be related with water vapor since no other volatile compounds were expected at this temperature. Evaporation of water started around 50 °C, but was observed during the whole heating ramp due to the high heating rate (100 °C /min) and the consequent short time (just 2 min). Interestingly, ZnO/AR contains a small amount of water that

was evaporated between 150 °C and 250 °C. The presence of water is caused by the hygroscopic nature of the ZnO and may be responsible for the slight densification observed at the beginning of the isothermal holding time.

After the cold sintering process, XRD was carried out on the samples consolidated by FAST/SPS at 150 MPa (Supplementary data 2), and the calculated crystallite size based on the analysis is shown in Table I. Table I shows also an overview of all the sintered samples, presenting the starting composition, the specific sintering conditions, the final density and the crystal sizes in the (100), (002) and (110) planes for each sample. Pure hexagonal wurzite phase of ZnO phase was obtained for all the compositions, and no background related to amorphous phase or other secondary crystalline phases were detected by XRD. ZnO/H<sub>2</sub>O presented broader peaks characteristic of nano-crystals, which enabled to calculate their primary grain sizes in the different crystallographic planes when values are lower than 100 nm. On the other hand, crystal size calculation could not be performed for ZnO/Ac-H<sub>2</sub>O, suggesting larger grains. According to the results, the crystal sizes in the planes (100), (002) and (110) increase as follow: ZnO powder < ZnO/H<sub>2</sub>O < ZnO/Ac-H<sub>2</sub>O. Interestingly, the grains grew preferentially in the crystallographic plane (002). The intensity of (002) peak for ZnO/Ac-H<sub>2</sub>O is rather low in comparison with the others, effect that was already observed and corresponds with the texturing due to the uniaxial pressure during the sintering process [15]. The measured crystal size was supported by SEM pictures of the fracture surfaces (Fig. 3). Homogeneous microstructures were observed for all the samples but different grain sizes were obtained. ZnO/H<sub>2</sub>O presents grain sizes below 100 nm, confirming the results measured by XRD (Table I). These grain size values are in good agreement with the observed for the ZnO/H<sub>2</sub>O reported by Dargatz et al.[15] at 50 MPa. In that

work, the mean crystalline size was 58.8 nm at relative density of 72%, observing a texturing effect from this density due to the applied pressure. However, ZnO/Ac-H<sub>2</sub>O exhibits larger elongated grains, with particle sizes > 500 nm, surrounded by smaller particles. The difference in grain size is just caused by the 0.5 wt.% of zinc acetate dissolved into the water as the other parameters remained equal.

Figure 4 shows the normalized densification rate as a function of effective pressure during the isothermal holding time at 250 °C for ZnO/H<sub>2</sub>O and ZnO/Ac-H<sub>2</sub>O. In Figure 4a the relative density was maintained constant at values of 0.80 and 0.82 for ZnO/H<sub>2</sub>O, meanwhile in Figure 4b the constant relative densities were 0.83 and 0.85 for ZnO/Ac-H<sub>2</sub>O. The calculated stress exponent  $n$  was practically constant for each composition at the given densities, 4.55 for ZnO/H<sub>2</sub>O and 2.68 for ZnO/Ac-H<sub>2</sub>O. These stress exponents indicate a combination of sintering mechanisms instead of one single mechanism, as expected for solid state sintering of ZnO. According to the literature and previous studies of some of the authors, grain boundary diffusion ( $n = 1$ ) is the densification mechanism of pure ZnO powder using FAST/SPS or HP [31], whereas the calculated values of the present work are very different and larger than 1, suggesting a high sensitivity to the applied pressure. Such non-linearity is usually attributed to other mechanisms such as plastic deformation ( $n > 3$ ) and/or grain boundary sliding ( $n = 1$  or 2) [1]. A classical densification by liquid phase sintering would also lead to a stress exponent of 1. Unfortunately, no stress exponent has been reported so far for Cold Sintering Process of any ceramic system, so the comparison with the literature is not possible. However, Funahashi et al.[20] reported recently a much lower activated energy of grain growth – 43 kJ/mol – of ZnO under CSP, indicating a genuine sintering process at these low temperatures.



### 3.2. Comparison with ~~warm~~ hand pressing with a heater holder

According to the low sintering temperature used in the present FAST/SPS experiments and the recently proposed CSP [19], the same compositions were consolidated under similar conditions using a ~~warm press~~ hand pressing with a heater holder. The uniaxial pressure was kept at 150 MPa, although tests at 300 MPa were also performed to characterize the effect of the pressure and to increase the final density. Unfortunately, no in-situ monitoring of the sample shrinkage was possible with this equipment, as in the studies on CSP published until now, so that in-situ dilatometry is not accessible. Final densities and crystal sizes of the sintered samples are also shown in Table I, and compared with the results obtained by FAST/SPS. ZnO/H<sub>2</sub>O sintered under FAST/SPS at 150 MPa and WP show different final density, 91.5 % and 87.9 %, respectively. The only difference between these two samples is the heating rate (100 °C/min and 20 °C/min for FAST/SPS and WP, respectively), which plays a key role for the retention of water. The other difference is the steel used for the die but no interaction is expected between the sample and the die. The fast heating rate allows to keep more water at higher temperatures in the compact to promote densification, whereas in the case of conventional heating rates water is evaporated, as already shown in FAST/SPS experiments [14][13]. Therefore, in order to enhance densification without increasing the amount of water in the sample the first approach was to increase the pressure from 150 MPa to 300 MPa, maintaining constant the initial content of water (1.6 wt.%). However, there was no further increase in density despite the higher pressure level, around 88 %. The second approach was to increase the content of water to compensate the early loss due to the lower heating rate. The initial content of water was doubled (3.2 wt.%) and the final density increased up to 93.4 %. Finally, ZnO was mixed with 3.2

wt.% of water and 0.5 wt.% of zinc acetate and sintered under the same conditions, achieving a final density of 94.0 %. The improvement is lower than expected, although the microstructure contains larger grains (Figure 5). Figure 5 shows the fracture surfaces of the ZnO compositions sintered by WP at 300 MPa. ZnO/H<sub>2</sub>O samples present homogeneous grain distributions with sizes below 100 nm, which were confirmed by XRD calculation (Table I). On the other hand, ZnO/Ac-H<sub>2</sub>O presented also a homogeneous grain size distribution but with larger grains, mainly in the crystallographic plane (002). This larger grain growth triggered by the presence of dissolved zinc acetate was already observed in the FAST/SPS experiments (Fig. 3).

### **3.3. Analysis of the defect formation by Kelvin Probe Force Microscopy**

The sintering of ZnO under mechanical pressure at low temperature is triggered by the presence of water in the compact and a possible transient water-based liquid phase, but the sintering mechanisms are still unclear. Defect formation and interfacial energies dictate the sintering behaviour of ZnO, and their modification by the presence of water could be determinant to understand the observed better sinterability. In previous works, some of the authors have reported the modification of point defects when water was present during the FAST/SPS sintering by using photoluminescence at low temperature (5 K) and electron paramagnetic resonance [14][15]. However, these techniques provide an overall value for the whole sample and the characterization of grain boundaries is not allowed. On the other hand, Kelvin Probe Force Microscopy (KPFM) is a scanning probe technique that enables the observation of the topography of a sample in combination with the surface potential at a high lateral resolution [32][33][34], leading to a mapping of the local changes in defect

concentrations and surface processes [32][35][36]. In the past, KPFM has already been applied to ZnO to confirm Schottky-behavior of metal contacts on ZnO nanowires [37] or to investigate defect gradients due to structural variations of the ZnO surface [38][39]. The technique has also already been successfully applied to characterize the electrochemical behavior of grain boundaries in chalcopyrite materials [40][41][42] with a similar approach as presented in this work. KPFM is performed in intermittent contact mode with the cantilever vibrating at its resonance frequency. Additionally, an AC potential is applied to the AFM tip. This potential changes in interaction with the sample. An additional external voltage  $U_{DC}$  compensates the surface potential difference between the sample and the probe tip [32]:

$$U_{KPFM} = \Delta\phi_{CPD} = -U_{DC} . \quad (6)$$

A surface plot of the potential  $-U_{DC}$  during the surface scan of the probe tip yields the KPFM image. The contact potential difference ( $\Delta\phi_{CPD}$ ) measured at the same time the difference of the work functions of the AFM tip ( $\phi_{tip}$ ) and the sample ( $\phi_{smp}$ ).

$$\Delta\phi_{CPD} = \frac{\phi_{tip} - \phi_{smp}}{-e} \quad (7)$$

where  $e$  is the elementary charge.

As the work function is proportional to the Fermi energy level of the tip and the sample, respectively, changes in the defect concentration of the sample can be detected, assuming the tip is not affected during the experiments. Therefore, KPFM could provide novel data to understand the sinterability at low temperatures of ZnO.

Figure 6 shows the topography and the relative surface potential of the three ZnO compositions sintered by FAST/SPS at 150 MPa. The topography images show homogenous microstructures with grains in the nanometer range for ZnO/AR (Fig. 6 a and b) and ZnO/H<sub>2</sub>O (Fig. 6 b and c). In both samples, grains and grain boundaries were well distinguishable. On the other hand, ZnO/Ac-H<sub>2</sub>O exhibits large heterogeneity regarding the grain sizes, presenting some grains in the range of  $> 1 \mu\text{m}$  and others below  $0.1 \mu\text{m}$  (Fig. 6 e and f). Using these images the particle size of the three ZnO samples was estimated using the lineal-intercept method with a correction factor of 1.56 for at least 250 grains per condition (Table II). These results are in concordance with the fractures surfaces of the samples (Fig. 3), although they are larger than the values obtained by XRD (Table I).

The surface potential difference ( $\Delta\Phi_{\text{SP}}$ ) between grains and grain boundaries (GB) was analyzed for each grain individually (Figure 7). A similar procedure has already been proposed by Sadewasser et al.[42], due to the fact, that each grain can have a slightly varying average surface potential due to the crystallite orientation. It has to be mentioned that only grain/GB-pairs, which we were able to identify unambiguously by the topography image and topography cross section, were measured.  $\Delta\Phi_{\text{SP}}$  was calculated using the mean surface potential of each grain and the lowest surface potential detected in the area of the grain boundary. The grains correspond with the grey areas, while the grain boundaries are the white zones in Figure 7 (areas without a clear identification of grain/GB-pair are also shown as white but they were not measured). These white zones include the space charge layer since the grain boundary itself is too small to be measured by the AFM tip, i. e. these are the “electrical grain boundaries” instead of the “crystallographic grain boundaries”. Nevertheless, the crystallographic grain

boundary can be located at the minimum height of the profile. ~~It has to be emphasized that only grains and grain boundaries which were unmistakably identifiable by the topography image and topography cross section were taken into account.~~

There are two main issues concerning the evaluation of the KPFM images: on the one hand, it is obvious that the KPFM measurements show a low signal/noise ratio which in many cases impedes an unequivocal definition of the average grain surface potential of the grains. ~~In addition,~~ On the other hand, as the AFM tip is broader (25 nm) than the grain boundary itself, the surface potential measured for the grain boundary is not the pure potential of the grain boundary itself [33][34], but a mixed signal of the grain boundary and adjacent space charge layer (defined above as electrical grain boundary) [42]. Therefore, we assume that the actual surface potential difference between grain and ~~of the~~ grain boundary core should be even lower than our measured values. As result of these problems to estimate the mean values of  $\Delta\Phi_{SP}$  for the three samples, which are shown in Table II, can only be taken as evidence for the Schottky barrier height within the samples but are not conclusive in themselves. To improve the credibility of the data, reproduction measurements were performed with the Cypher AFM. Results in a similar range of  $\Delta\Phi_{SP}$  were obtained.

As can be seen from Table II, ZnO/H<sub>2</sub>O presents a higher surface potential difference than ZnO/AR, ~~showing~~ suggesting an ~~clear~~ increase of the defect concentration on the surface of the ZnO/H<sub>2</sub>O. On the other hand, ZnO/Ac-H<sub>2</sub>O presents the lowest surface potential difference so the addition of acetate reduced the defect concentration in the final material. Nevertheless,

this sample exhibited larger grains so the measured surface is not the initial surface – in which is expected to have high defect concentration – since grain growth process occurred.

In order to confirm the results obtained by KPFM, impedance spectroscopy was used for the different consolidated ZnO samples. Figure 8 shows the bulk, boundary and total conductivity calculated from impedance spectroscopy measurements of the three samples between -20 and 90 °C. From the impedance measurements it was deduced that all the samples suffer from a more or less pronounced deterioration during heating: between the measurement from -20 to 90 °C and the subsequent measurement in the opposite direction there was a significant hysteresis. Even during the measurement in up-direction, a change of the respective contributions of grains and grain boundaries in the impedance spectra and hence a deviation of the conductivity from the standard Arrhenius behavior was found already at relatively low temperatures (already around 30 °C for ZnO/Ac-H<sub>2</sub>O compared to about 60 °C for ZnO/H<sub>2</sub>O).

Therefore, only the measurements in the up-direction are shown in Fig. 8. The dashed lines show the onset of the non-Arrhenius behavior in the samples. The activation energies for the respective samples, which are shown in Tab. III, and the space charge potentials, which are shown in Tab. II, were calculated from -20 °C to the indicated beginning of the non-Arrhenius behavior of the samples. By further comparing the graphs in Fig. 8, it can be observed that ZnO/Ac-H<sub>2</sub>O shows the highest total conductivity and also the separate contributions of bulk and grain boundary conductivity are significantly enhanced with respect to ZnO/AR and ZnO/H<sub>2</sub>O. In contrast to the idea that H<sub>2</sub>O addition should lead to a donor doping effect in ZnO, which should increase the total conductivity, ZnO/H<sub>2</sub>O shows a lower conductivity than the

pure sample ZnO/AR, even though ZnO/AR also has a lower density and a higher grain boundary/grain ratio.

Previous findings [14] showed that especially the grain boundary transport was affected by H<sub>2</sub>O loss during a heating experiment (cf. Tab. III). Therefore, a strong influence of the different sintering procedures especially on the grain boundary transport was expected. However, by comparing the activation energies for bulk ( $E_{A, b}$ ), grain boundary ( $E_{A, GB}$ ) and total transport ( $E_{A, tot}$ ) in Table III, it becomes obvious that especially the bulk transport is affected by the addition of water and acetate during sintering, leading to a strong decrease of the activation energy.

The space charge potential values  $\Delta\Phi_{imp}$  which were calculated from the impedance measurements according to eq. (1) are shown in Tab II. The potential values show a similar trend like already observed from the KPFM measurements: the potential barrier for ZnO/AR is slightly lower than for ZnO/H<sub>2</sub>O, meanwhile the calculated potential barrier for ZnO/Ac-H<sub>2</sub>O is distinctly smaller. Interestingly, the values of  $\Delta\Phi_{imp}$  and  $\Delta\Phi_{sp}$  are comparable, following the same trend and confirming the results obtained by KPFM. This can be attributed to the fact, that KPFM measurements were performed in a single-pass measurement method (5500 AFM) and the reproduction measurements with the Cypher AFM were performed with a very low distance between tip and sample (typically less than 10 nm). Obviously, this measurement method allows for a relatively correct assumption of the surface potential difference between bulk and grain boundary apart from the low signal/noise ratio.

#### **4. Discussion**

It has been demonstrated that a combination of pressure and low water contents can lead to full densification of nanocrystalline ZnO at low temperatures (250 °C). This effect was already observed by some of the authors at higher temperatures (400 °C) [14][15], although the involved detailed mechanisms were not fully understood. In these studies, densification already started at 250 °C but the relative density was rather low (~ 60 %) due to the lower uniaxial pressure used (50 MPa). In the current work, the reduction of the maximal temperature was achieved by increasing the compressive stress, which was done by using alternative FAST/SPS tools based on steel (100 MPa - 150 MPa) instead of graphite. The increase of the compressive stress plays a determinant role during all the steps of densification: i) the compaction of the green bodies, ii) the onset temperature of densification and densification rate and iii) final density (Fig. 1 and 2). The reduction of the onset temperature of densification is determinant, especially for enabling fast thermal cycling at low temperature (heating process was just 7 min for these FAST/SPS experiments). The presence of acetate even reinforces this triple effect, with especial consideration to the fact that the onset temperature was decreased down to 25 °C. Certainly, this strong reduction enables better sinterability and higher final densities. The measured stress exponents suggest a non-linear relationship between densification rate and applied pressure for a given density (Fig. 4), and imply different sintering mechanisms than reported for solid state sintering of ZnO by FAST/SPS [31]. In addition, the dramatic effect of pressure on the final density can be easily observed (Fig. 1 and Table I). The controlling mechanism is not purely grain boundary diffusion or even liquid phase sintering since  $n > 1$ . The calculated values suggest a complex phenomenon where different mechanisms could take part, including dislocation motion and grain boundary sliding.



Large reduction of the sintering temperature using water as sintering aid has also been reported by the recently labelled “cold sintering process” [17][16][18]. However, CSP was carried out under larger contents of water (4 – 30 wt.%) and the related mechanisms were hypothesized as solution-precipitation liquid-phase assisted sintering. Due to the low temperature and the precipitation phenomena of an amorphous phase, CSP often requires a further annealing treatment at higher temperature ( $\sim 700 - 900\text{ }^{\circ}\text{C}$ ) to crystallize the ceramic compound [19]. Nevertheless, this further thermal treatment was not required for the ZnO [20]. In the present work, we show that water plays a key role, but since the low amount of water (only 1.7 wt.%) is not enough to promote solution-precipitation as main densification mechanism, other mechanisms need to be activated. It is important to remark that solution-precipitation might be the main mechanism during the presence of water, as it is reported by several authors. However, water is only present during the first part of the densification since water is evaporated from the system during the heating ramp (Supplementary data 1) when low content of water is used. Therefore, in the last step of the cold sintering process – during the isothermal holding time –, which corresponds with relative densities  $> 75\%$ , solution-precipitation is unlikely. Previous calculations showed that this low amount of water implies just two nanolayer of water ( $4.5\text{ }\text{\AA}$ ) covering the ZnO nanoparticles, i.e. building more an interface than an interphase [14]. Slight dissolution of ZnO in water is well known, and it is required to promote this process. The dissolution process can be enhanced by acidifying the water media, as it was carried out by Funahashi et al. [20] to trigger CSP using acetic acid, or in this work by using zinc acetate. Enhancement of the dissolution process by the acetate can be easily observed in the strong reduction of the onset temperature for densification (Figure 2).

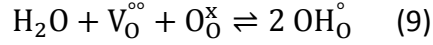
This interaction between the particle surface and the water is required, as it is also mandatory between the ceramic powder and the second phase in liquid phase sintering [1]. As a result,  $\text{Zn}^{2+}$  and  $\text{O}^{2-}$  ions are dissolved in this interface originated from the presence of water between the particles.

Grain boundaries in ZnO can be represented by a Schottky barrier model [27]. In this model, negative charges are agglomerated directly at the grain boundary (increased concentration of cation vacancies  $V'_{\text{Zn}}$  and  $V''_{\text{Zn}}$ ), while a positively charged space charge layer surrounds the grain boundary. The positive charge can be contributed by an increased concentration of oxygen vacancies ( $V^{\circ}_{\text{O}}, V^{\circ\circ}_{\text{O}}$ ) and zinc on interstitial lattice sites ( $\text{Zn}^{\circ}_{\text{i}}, \text{Zn}^{\circ\circ}_{\text{i}}$ ) as well as impurity donor cations [27][43]. These cations can either be impurities like Bi, Sb ( $D^{\circ}_{\text{Zn}}$ ) etc. but it has also been confirmed that water or rather protons work as shallow donors in ZnO ( $\text{OH}^{\circ}_{\text{O}}$ ) [44][45][46], increasing the electronic conductivity. An increase of the proton concentration should therefore lead to an increase of positive charge in the space charge region and also to an increase of negative charge in the direct vicinity of the grain boundary to keep the overall neutrality. At the same time, the surface potential of the whole grain should be increased with respect to the surface potential of the grain boundary, assuming a more or less even distribution of donor dopant within the grain apart from the space charge layer (Fig. 9).

The electroneutrality equation for the ZnO system is:

$$e + [V'_{\text{Zn}}] + [V''_{\text{Zn}}] = h + [V^{\circ}_{\text{O}}] + [V^{\circ\circ}_{\text{O}}] + [\text{Zn}^{\circ}_{\text{i}}] + 2[\text{Zn}^{\circ\circ}_{\text{i}}] + [D^{\circ}_{\text{Zn}}] + [\text{OH}^{\circ}_{\text{O}}] \quad (8)$$

Water can be incorporated as hydroxyl ions on oxygen vacancy sites (eq. 9).



Once in the lattice, protons are able to move by a hopping mechanism from oxygen atom to oxygen atom. In ZnO, approximately half of adsorbed water molecules dissociate into  $\text{H}^+$  and  $\text{OH}^-$ , diffusing through the crystal structure and/or bonding with the oxygen atoms as shown by the combination of different techniques such as He-atom scattering (HAS), low-energy electron diffraction (LEED), scanning tunneling microscopy (STM) and He-thermal desorption spectroscopy (He-TDS) [47][48]. Thus, protons or hydroxyl ions from the dissociation of water diffuse into the ZnO crystal structure generating defects and increasing the surface potential difference between grains and grain boundaries (Fig. 6 and 7, and Table II). These grain boundaries/interfaces with high defect chemistry and high gradient potential are the driving force for the densification at low temperature due to the following equation:

$$\frac{N_d}{N} = \exp\left(\frac{-Q_p}{KT}\right) \quad (10)$$

Where  $N_d$  is the number of defects,  $N$  is the number of potential defect sites, and  $Q_p$  the activation energy.

The high defect concentration at grain boundaries with high potential could be the responsible of the reduction of ~~reduces~~ the activation energy of the atomic diffusion, promoting the sintering at low temperature.

Commonly, adsorption of water on the surface of nanoparticles decreases the surface energy [49], lowering the sinterability of the particles. However, in the current case the water is dissociated and the remaining excess of water is eliminated from the system by evaporation

(Supplementary data 1). As a result, after an initial beneficial effect of water – larger compaction of green bodies due to reduction of friction, dissolution of some atoms on the surface of the particles, generation of local defects at the interface, and increment of the surface potential – residual water is eliminated, leaving behind the particles with high surface energy to sinter at low temperature. As the process is controlled by the surface, nanoparticles are beneficial to maximize the ratio surface/grain. In addition, the free water (remaining water that was not dissociated) has to vanish from the system before complete closure of porosity to avoid the formation of a second phase between the grains and to finish the densification process.

According to our analysis, the adsorbed water has five main effects: i) better initial packing due to reduction of interparticle friction, ii) dissolution of  $\text{Zn}^{2+}$  and  $\text{O}^{2-}$  ions on the surface particle, iii) defect formation due to diffusion of  $\text{H}^+$  and  $\text{OH}^-$  ions into the ZnO crystals, iv) formation of a highly defective diffusion path between grains, and v) carbonate elimination. It has to be mentioned that pressure plays also a critical role since it increases the green density, the contact between the particles and their reorientation and sliding, triggering so new densification mechanisms which also lead to higher densification rates.

The system containing zinc acetate is slightly different, because the modification of the pH of the added water enhances the water effect. ~~although the sintering mechanisms are the same (Fig 4).~~ First, solubility of ZnO is enhanced in acidic pH conditions, so solution-precipitation stage can start at lower temperatures. This is easily observed for the onset temperature for densification (Figure 2), as well as already observed in ZnO by CSP [20]. Furthermore, the

incorporation of zinc acetate promotes larger dissolution of  $\text{Zn}^{2+}$  and  $\text{O}^{2-}$  ions into the water boundary layer, as well as more  $\text{Zn}^{2+}$  ions by the dissolution of the zinc acetate. According to the information provided by KPFM, XRD and the obtained microstructure, and previous investigation by some of the authors [24][25], epitaxial grain growth on the surface of the ZnO particles takes place when zinc acetate is incorporated. The crystals grow in the preferential (002) crystallographic plane, which may be related with precipitation mechanisms. As a result, the microstructure of ZnO/Ac-H<sub>2</sub>O exhibited larger grains (Fig. 3 e, f) than ZnO/H<sub>2</sub>O. These larger grains presented lower amount of defects so the final surface potential is lower than the samples sintered without acetate (Figure 6 and Table II). Nevertheless, this lower surface potential was measured once that the grain growth occurred so it cannot be directly compared with the samples with negligible grain growth.

Sintering at low temperatures using adsorbed water has been demonstrated using FAST/SPS, but it is not restricted to this technique, as it has been shown using a ~~warm~~ hand press with a heater holder due to the low required temperature. In a ~~warm~~ hand press the initial content of water has to be larger to compensate its evaporation induced by the lower heating rates. It is obvious that a standard ~~warm~~ hand press does not allow to have controlled experiments but is simpler and cheaper than a FAST/SPS machine. Ideally the environment for water-assisted sintering would be a partially confined atmosphere (with a controlled water vapor partial pressure) because on the one hand enough water should remain at the surface of the particles but on the other hand surplus water has to be removed out of the specimen in order to have complete densification. Nevertheless, high homogeneous dense materials containing mean grain sizes below 100 nm were obtained.

## 5. Conclusions

ZnO has been highly densified (> 90 % theoretical density) at an ultra-low temperature of 250°C by the combined effect of pressure and adsorbed water using a FAST/SPS. To promote the densification at low temperature, steel tools were used in the FAST/SPS to increase the pressure up to 150 MPa. Furthermore, similar enhanced sintering behavior has been also demonstrated using a hand ~~warm~~ press at 250 °C and uniaxial pressure up to 300 MPa.

The applied pressure plays a critical role to increase the green body density, decrease the onset temperature of densification and to increase the final density of the ZnO samples. A new dependence between densification and stress has been measured, as testified by a value of stress exponent larger than one. In contrast to standard FAST/SPS, grain boundary diffusion (or as postulated for cold sintering liquid phase sintering) is not the controlling mechanism for densification.

Regarding the addition of water, small amounts (1.7 wt.%) are just required because the process is dictated by the adsorbed water at the surface of particles. In case of excess of water (non-absorbed), it is evaporated during the thermal treatment. The main effect of the adsorbed water is: i) better initial packing due to reduction of interparticle friction, ii) dissolution of  $\text{Zn}^{2+}$  and  $\text{O}^{2-}$  ions on the surface particle, iii) defect formation due to diffusion of  $\text{H}^+$  and  $\text{OH}^-$  ions into the ZnO crystals, iv) formation of a highly defective diffusion path between grains, and v) carbonate elimination. The presence of acetate into the water modifies the pH, enhancing these effects. As a result, the grain boundary area presents high defect chemistry with high

potential due to the formation of defects, reducing the activation energy of the atomic diffusion and leading to sintering the material at low temperature.

## References

- [1] M.N. Rahaman, Ceramic Processing and Sintering, Second edi, Marcel Dekker Inc., New York, 2003.
- [2] V. Zamora, a. L. Ortiz, F. Guiberteau, M. Nygren, Crystal-size dependence of the spark-plasma-sintering kinetics of ZrB<sub>2</sub> ultra-high-temperature ceramics, J. Eur. Ceram. Soc. 32 (2012) 271–276.
- [3] M. Thompson, W.G. Fahrenholtz, G. Hilmas, Effect of Starting Particle Size and Oxygen Content on Densification of ZrB<sub>2</sub>, J. Am. Ceram. Soc. 94 (2011) 429–435.
- [4] R.M. German, P. Suri, S.J. Park, Review: liquid phase sintering, J. Mater. Sci. 44 (2009) 1–39.
- [5] O. Guillon, J. Gonzalez-Julian, B. Dargatz, T. Kessel, G. Schierning, J. Räthel, M. Herrmann, Field-Assisted Sintering Technology/Spark Plasma Sintering: Mechanisms, Materials, and Technology Developments, Adv. Eng. Mater. 16 (2014) 830–849.
- [6] M. Cologna, B. Rashkova, R. Raj, Flash sintering of nanograin zirconia in <5 s at 850 C, J. Am. Ceram. Soc. 93 (2010) 3556–3559.
- [7] N. Yamasaki, K. Yanagisawa, A hydrothermal hot-pressing method: apparatus and application, J. Mater. Sci. Lett. 5 (1986) 355–356.
- [8] K. Yanagisawa, Q. Feng, N. Yamasaki, Preparation of Ceramics by Hydrothermal Hot-pressing, High Press. Res. 20 (2001) 343–349.



- [9] K. Yanagisawa, K. Ioku, N. Yamasaki, Formation of Anatase Porous Ceramics by Hydrothermal Hot-Pressing of Amorphous Titania Spheres, *J. Am. Ceram. Soc.* 80 (1997) 1303–1306.
- [10] J. Li, T. Hashida, Preparation of hydroxyapatite ceramics by hydrothermal hot-pressing method at 300 °C, *J. Mater. Sci.* 42 (2007) 5013–5019.
- [11] S. Takezoe, K. Hosoi, M. Tajika, Y. Yamasaki, A. Nakahira, Syntheses of Bulky Y-Zeolite by Hydrothermal Hot-Pressing (HHP) Technique, *Key Eng. Mater.* 317–318 (2006) 97–100.
- [12] P. De Silva, L. Bucea, V. Sirivivatnanon, D.R. Moorehead, Carbonate binders by “cold sintering” of calcium carbonate, *J. Mater. Sci.* 42 (2007) 6792–6797.
- [13] S. Schwarz, A.M. Thron, J. Rufner, K. Van Benthem, O. Guillon, Low Temperature Sintering of Nanocrystalline Zinc Oxide : Effect of Heating, *J. Am. Ceram. Soc.* 95 (2012) 2451–2457.
- [14] B. Dargatz, J. Gonzalez-Julian, M. Bram, P. Jakes, A. Besmehn, L. Schade, R. Röder, C. Ronning, O. Guillon, FAST/SPS sintering of nanocrystalline zinc oxide-Part I: Enhanced densification and formation of hydrogen-related defects in presence of adsorbed water, *J. Eur. Ceram. Soc.* 36 (2016) 1207–1220.
- [15] B. Dargatz, J. Gonzalez-Julian, M. Bram, Y. Shinoda, F. Wakai, O. Guillon, FAST/SPS sintering of nanocrystalline zinc oxide-Part II: Abnormal grain growth, texture and grain anisotropy, *J. Eur. Ceram. Soc.* 36 (2016) 1221–1232.
- [16] J. Guo, H. Guo, A.L. Baker, M.T. Lanagan, E.R. Kupp, G.L. Messing, C.A. Randall, Cold

Sintering: A Paradigm Shift for Processing and Integration of Ceramics, *Angew. Chemie.* (2016).

- [17] J. Guo, S.S. Berbano, H. Guo, A.L. Baker, M.T. Lanagan, C.A. Randall, Cold Sintering Process of Composites: Bridging the Processing Temperature Gap of Ceramic and Polymer Materials, *Adv. Funct. Mater.* 26 (2016) 7115–7121.
- [18] H. Guo, A. Baker, J. Guo, C.A. Randall, Protocol for ultralow temperature ceramic sintering: an integration of nanotechnology and Cold Sintering Process, *ACS Nano.* 10 (2016) 10606–10614.
- [19] H. Guo, A. Baker, J. Guo, C.A. Randall, D. Johnson, Cold Sintering Process: A Novel Technique for Low-Temperature Ceramic Processing of Ferroelectrics, *J. Am. Ceram. Soc.* 99 (2016) 3489–3507.
- [20] S. Funahashi, J. Guo, H. Guo, K. Wang, A.L. Baker, K. Shiratsuyu, C.A. Randall, Demonstration of the Cold Sintering Process Study for the Densification and Grain Growth of ZnO Ceramics, *J. Am. Ceram. Soc.* 100 (2017) 546–553.
- [21] S.S. Berbano, J. Guo, H. Guo, M.T. Lanagan, C.A. Randall, Cold sintering process of  $\text{Li}_{1.5}\text{Al}_{0.5}\text{Ge}_{1.5}(\text{PO}_4)_3$  solid electrolyte, *J. Am. Ceram. Soc.* 100 (2017) 2123–2135.
- [22] M. Väätäjä, H. Kähäri, J. Juuti, H. Jantunen,  $\text{Li}_2\text{MoO}_4$ -based composite ceramics fabricated from temperature- and atmosphere- sensitive MnZn ferrite at room temperature, *J. Am. Ceram. Soc.* 100 (2017) 3626–3635.
- [23] J. Nie, Y. Zhang, J.M. Chan, R. Huang, J. Luo, Water-assisted flash sintering: Flashing ZnO

- at room temperature to achieve ~ 98% density in seconds, *Scr. Mater.* 142 (2018) 79–82.
- [24] B. Dargatz, J. Gonzalez-Julian, O. Guillon, Improved compaction of ZnO nano-powder triggered by the presence of acetate and its effect on sintering, *Sci. Technol. Adv. Mater.* 16 (2015).
- [25] B. Dargatz, J. Gonzalez-Julian, O. Guillon, Anomalous coarsening of nanocrystalline zinc oxide particles in humid air, *J. Cryst. Growth.* 419 (2015) 69–78.
- [26] J. Fleig, The grain boundary impedance of random microstructures: Numerical simulations and implications for the analysis of experimental data, *Solid State Ionics.* 150 (2002) 181–193.
- [27] T.K. Gupta, W.G. Carlson, A grain boundary defect model for instability stability of a ZnO varistor, *J. Mater. Sci.* 20 (1985) 3487–3500.
- [28] S. Kim, J. Maier, On the Conductivity Mechanism of Nanocrystalline Ceria, *J. Electrochem. Soc.* 149 (2002) J73.
- [29] J. Langer, M.J. Hoffmann, O. Guillon, Direct comparison between hot pressing and electric field-assisted sintering of submicron alumina, *Acta Mater.* 57 (2009) 5454–5465.
- [30] J.M. Montes, F.G. Cuevas, J. Cintas, A new expression for the effective pressure on powders under compression, *Comput. Mater. Sci.* 36 (2006) 329–337.
- [31] J. Langer, M.J. Hoffmann, O. Guillon, Electric field-assisted sintering and hot pressing of semiconductive zinc oxide: A comparative study, *J. Am. Ceram. Soc.* 94 (2011) 2344–

2353.

- [32] W. Melitz, J. Shen, A.C. Kummel, S. Lee, Kelvin Probe Force microscopy and its application, *Surf. Sci. Rep.* 66 (2011) 1–27.
- [33] U. Zerweck, C. Loppacher, T. Otto, L. Grafstroem, M. Lukas, Accuracy and resolution limits of Kelvin Probe Force microscopy, *Phys. Rev. B.* 71 (2005) 125424.
- [34] H. Jacobs, P. Leuchtmann, J. Homan, A. Stemmer, Resolution and contrast in Kelvin Probe Force microscopy, *J. Appl. Phys.* 84 (1998) 1168.
- [35] K. Neuhaus, M. Bernemann, K. Vels Hansen, T. Jacobsen, G. Ulbrich, E. Heppke, M. Paun, M. Lerch, H. Wiemhoefer, Study of the Polarization Behavior of  $\text{Ce}_{0.9}\text{Gd}_{0.1}\text{O}_{2-\delta}$  Single Crystals below 350° C to Room Temperature, *J Electrochem Soc.* 163 (2016) H1179.
- [36] K. Neuhaus, F. Schulze-Küppers, S. Baumann, G. Ulbrich, M. Lerch, H. Wiemhoefer, Scanning probe microscopy polarization experiments with polycrystalline  $\text{Ce}_{0.8}\text{Gd}_{0.2-x}\text{Pr}_x\text{O}_{2-\delta}$  and  $\text{Ce}_{0.8}\text{Y}_{0.2}\text{O}_{2-\delta}$  single crystals at room temperature, *Solid State Ionics.* 288 (2016) 325.
- [37] B. Bercu, W. Geng, O. Simonetti, S. Kostcheev, C. Sartel, V. Sallet, G. Léron del, M. Molinari, L. Giraudet, C. Couteau, Characterizations of Ohmic and Schottky-behaving contacts of a single ZnO nanowire, *Nanotechnology.* 24 (2013) 415202.
- [38] T.A. Merz, D.R. Douth, T. Bolton, Y. Dong, L.J. Brillson, Nanostructure growth-induced defect formation and band bending at ZnO surfaces, *Surf. Sci.* 605 (2011) L20–L23.

- [39] E. De Lucas-Gil, J.J. Reinoso, K. Neuhaus, L. Vera-Londono, M. Martín-González, J.F. Fernández, F. Rubio-Marcos, Exploring New Mechanisms for Effective Antimicrobial Materials: Electric Contact-Killing Based on Multiple Schottky Barriers, *ACS Appl. Mater. Interfaces*. 9 (2017) 26219–26225.
- [40] S. Sadewasser, T. Glatzel, S. Schuler, S. Nishiwaki, R. Kaigawa, M.C. Lux-Steiner, Kelvin probe force microscopy for the nano scale characterization of chalcopyrite solar cell materials and devices, *Thin Solid Films*. 431–432 (2003) 257–261.
- [41] D. Fuertes Marron, S. Sadewasser, A. Meeder, T. Glatzel, M.C. Lux-Steiner, Electrical activity at grain boundaries of Cu(In,Ga)Se<sub>2</sub> thin films, *Phys. Rev. B - Condens. Matter Mater. Phys.* 71 (2005) 1–4.
- [42] C. Leendertz, F. Streicher, M.C. Lux-Steiner, S. Sadewasser, Evaluation of Kelvin probe force microscopy for imaging grain boundaries in chalcopyrite thin films, *Appl. Phys. Lett.* 89 (2006) 2004–2007.
- [43] A.F. Kohan, G. Ceder, D. Morgan, C. Van de Walle, First-principles study of native point defects in ZnO, *Phys. Rev. B*. 61 (2000) 15019.
- [44] S. Hofmann, A. Hoftstaetter, F. Lieter, H. Zhou, F. Henecker, B. Meyer, S. Orlinskii, J. Schmidt, P. Baranov, Hydrogen: A Relevant Shallow Donor in Zinc Oxide, *Phys Rev Lett.* 88 (2002) 45504.
- [45] C. Van de Walle, Hydrogen as a cause of doping in zinc oxide, *Phys Rev Lett.* 85 (2000) 1012.

- [46] A. Janotti, C. Van de Walle, Fundamentals of zinc oxide as a semiconductor, Rep Prog Phys. 72 (2009) 126501.
- [47] C. Woell, The chemistry and physics of zinc oxide surfaces, Prog. Surf. Sci. 82 (2007) 55–120..
- [48] B. Meyer, D. Marx, O. Dulub, U. Diebold, M. Kunat, D. Langenberg, Partial Dissociation of Water Leads to Stable Superstructures on the Surface of Zinc Oxide, Angew. Chemie. 43 (2004) 6641–6645.
- [49] D. V. Quach, A.R. Bonifacio, R.H.R. Castro, Water adsorption and interface energetics of zinc aluminate spinel nanoparticles: Insights on humidity effects on nanopowder processing and catalysis, J. Mater. Res. 28 (2013) 2004–2011.

## Figure Caption

**Fig. 1.** Densification curves for the three types of ZnO samples under uniaxial pressures of a) 100 MPa, b) 125 MPa, and c) 150 MPa

**Fig. 2.** Onset temperature of densification as a function of the applied pressure in the FAST/SPS for ZnO/H<sub>2</sub>O. Value at 50 MPa is extracted from [14]

**Fig. 3.** SEM micrographs of the fracture surfaces of a) and b) ZnO/H<sub>2</sub>O, and c) and d) ZnO/Ac-H<sub>2</sub>O at 150 MPa

**Fig. 4.** Determination of stress exponent  $n$  at a given density between 0.80 and 0.85 for a) ZnO/H<sub>2</sub>O and b) ZnO/Ac-H<sub>2</sub>O.

**Fig. 5.** SEM micrographs of the fracture surfaces of a) ZnO/H<sub>2</sub>O with 1.6 wt.% H<sub>2</sub>O, b) ZnO/H<sub>2</sub>O with 3.2 wt.% H<sub>2</sub>O, and c) ZnO/Ac and 3.2 wt.% water sintered in the ~~warm~~ hand pressing at 300 MPa

**Fig. 6.** Topography and surface potential of a) and b) ZnO/AR, c) and d) ZnO/H<sub>2</sub>O, and e) and f) ZnO/Ac-H<sub>2</sub>O at 150 MPa in the FAST/SPS

**Fig. 7.** Surface potential difference  $\Delta\Phi_{sp}$  between grains and grain boundaries for a) ZnO/AR, b) ZnO/H<sub>2</sub>O, and c) ZnO/Ac-H<sub>2</sub>O

**Fig. 8.** Bulk, corrected grain boundary, and total conductivity of a) ZnO/AR, b) ZnO/H<sub>2</sub>O, and c) ZnO/Ac-H<sub>2</sub>O. Values calculated from impedance spectroscopy measurements in air.

**Fig. 9.** Scheme of the water adsorbed effect on the surface potential distribution of ZnO

## Tables

	Starting composition			Sintering conditions			Microstructure			
Technique	Composition	Water content (wt.%)	ZnAc content (wt.%)	Heating rate (°C/min)	Pressure (MPa)	Holding time (min)	Relative Density (%)	Crystal size (100) (nm)	Crystal size (002) (nm)	Crystal size (110) (nm)
FAST/SPS	ZnO/AR	-	-	100	100	5	57.9			
	ZnO/H2O	1.6	-	100	100	5	84.1			
	ZnO/Ac-H2O	1.6	0.5	100	100	5	88.3			
	ZnO/H2O	1.6	-	100	125	5	86.8			
	ZnO/Ac-H2O	1.6	0.5	100	125	5	93.4			
	ZnO/H2O	1.6	-	100	150	5	91.8	48	78	46
	ZnO/Ac-H2O	1.6	0.5	100	150	5	97.3	> 100	> 100	> 100
Hand press	ZnO/H2O	1.6	-	20	150	5	87.9	39	52	42
	ZnO/H2O	1.6	-	20	300	5	88.0	39	52	42
	ZnO/H2O	3.2	-	20	300	5	93.4	42	68	46
	ZnO/Ac-H2O	3.2	0.5	20	300	5	94.0	47	91	50

Table I. Starting composition, sintering conditions and microstructure of the ZnO samples sintered at 250 °C by FAST/SPS and hand pressing.



Composition	Mean particle size (nm)	$\Delta\Phi_{SP} / V$	$\Delta\Phi_{imp} / V$
ZnO/AR	$90 \pm 40$	$0.108 \pm 0.038$	$0.08 \pm 0.02$
ZnO/H2O	$183 \pm 80$	$0.136 \pm 0.054$	$0.11 \pm 0.01$
ZnO/Ac-H2O	$246 \pm 160$	$0.080 \pm 0.038$	$0.04 \pm 0.03$

Table II. Measured mean particle size, calculated average  $\Delta\Phi_{SP}$  by KPFM, and space charge potential calculated from impedance measurements  $\Delta\Phi_{imp}$  for the three different ZnO compositions.

Sample	$E_{A,b} / eV$	$E_{A,GB} / eV$	$E_{A,tot} / eV$
ZnO/AR	$0.41 \pm 0.03$	$0.24 \pm 0.01$	$0.25 \pm 0.01$
ZnO/H2O	$0.22 \pm 0.05$	$0.46 \pm 0.05$	$0.46 \pm 0.05$
ZnO/Ac-H2O	$0.15 \pm 0.01$	$0.21 \pm 0.03$	$0.21 \pm 0.03$
ZnO after 2 h at 100 °C [14]	$0.32 \pm 0.04$	$0.32 \pm 0.04$	$0.24 \pm 0.04$

Table III. Activation energies for bulk, grain boundary and total transport calculated from impedance measurements. Previously published data [14] for a ZnO sample prepared at 400 °C under aqueous conditions are shown for comparison.